MIT Libraries | DSpace@MIT

MIT Open Access Articles

Structure-Guided Directed Evolution of Highly Selective P450-Based Magnetic Resonance Imaging Sensors for Dopamine and Serotonin

Massachusetts Institute of Technology

Structure-Guided Directed Evolution of Highly Selective P450-based Magnetic Resonance Imaging Sensors for Dopamine and Serotonin

Eric M. Brustad[1], **Victor S. Lelyveld**[2], **Christopher D. Snow**[1], **Nathan Crook**[1], **Sang Taek Jung**[1], **Francisco M. Martinez**[5], **Timothy J. Scholl**[5], **Alan Jasanoff**[2,4,*], and **Frances H. Arnold**[1,*]

[1]Division of Chemistry and Chemical Engineering, California Institute of Technology, Pasadena, CA, USA

[2]Department of Biological Engineering, Massachusetts Institute of Technology, Cambridge, MA, USA

[3]Department of Brain and Cognitive Sciences, Massachusetts Institute of Technology, Cambridge, MA, USA

[4]Department of Nuclear Science and Engineering, Massachusetts Institute of Technology, Cambridge, MA, USA

[5]Department of Physics and Astronomy, University of Western Ontario, London, ON, Canada

Abstract

New tools that allow dynamic visualization of molecular neural events are important for studying the basis of brain activity and disease. Sensors that permit ligand-sensitive magnetic resonance imaging (MRI) are useful reagents due to the non-invasive nature and good temporal and spatial resolution of MR methods. Paramagnetic metalloproteins can be effective MRI sensors due to the selectivity imparted by the protein active site and the ability to tune protein properties using techniques such as directed evolution. Here we show that structure-guided directed evolution of the active site of the cytochrome P450 BM3 heme domain (BM3h) produces highly selective MRI probes with sub-micromolar affinities for small molecules. We report a new, high affinity dopamine sensor as well as the first MRI reporter for serotonin, with which we demonstrate quantification of neurotransmitter release *in vitro*. We also present a detailed structural analysis of evolved BM3h lineages to systematically dissect the molecular basis of neurotransmitter binding affinity, selectivity, and enhanced MRI contrast activity in these engineered proteins.

*Corresponding Authors: Frances H. Arnold, *frances@cheme.caltech.edu;* (626) 395-4162, Department of Chemistry and Chemical Engineering, California Institute of Technology, 1200 E. California Blvd. MC 210-41, Pasadena, CA. 91125, Alan Jasanoff, *jasanoff@mit.edu*.

Publisher's Disclaimer: This is a PDF file of an unedited manuscript that has been accepted for publication. As a service to our customers we are providing this early version of the manuscript. The manuscript will undergo copyediting, typesetting, and review of the resulting proof before it is published in its final citable form. Please note that during the production process errors may be discovered which could affect the content, and all legal disclaimers that apply to the journal pertain.

Competing Interest Statement
The authors declare no competing financial interests.

Accession codes. Atomic coordinates and structure factors for the reported crystal structures have been deposited with the Protein Data Bank (PDB) under the following accession codes - PDB ID: **4DTY** (BM3h-8C8), **4DTW** (BM3h-8C8:5HT), **4DTZ** (BM3h-8C8:DA), **4DU2** (BM3h-B7), **4DUC** (BM3h-2G9), **4DUF** (BM3h-2G9:5HT), **4DUD** (BM3h-2G9C6), **4DUE** (BM3h-2G9C6:5HT), **4DUA** (BM3h-9D7), **4DUB** (BM3h-9D7:DA). Accessibility has been designated 'for immediate release upon publication'.

Keywords

Directed evolution; Cytochrome P450; MRI contrast agents; neurotransmitter; Biosensors

INTRODUCTION

The exploitation of paramagnetic metalloproteins as magnetic resonance imaging (MRI) contrast agents is a promising direction for molecular imaging. Unlike traditional organometallic chelates, metalloproteins are amenable to protein engineering strategies that tune biophysical properties and molecular interactions. Endogenous metalloproteins such as ferritin already play a significant role in tissue and disease-specific MRI contrast differences[1], and ectopic expression has been shown to produce artificial contrast enhancement. Protein-based contrast agents can also be delivered exogenously using invasive or noninvasive means, even to the brain.[4] Ligand-dependent MRI contrast agents enable imaging of molecular events in the body, offering the possibility of improving on traditional approaches to functional MRI, which monitor physiological events only via changes in blood flow[5]. In the brain, metalloprotein-based probes that are engineered to respond to neurochemicals could be particularly useful, by providing direct molecular readouts associated with normal neural activity or dysregulation of chemical signaling in disease[6].

The bacterial cytochrome P450-BM3 heme domain (BM3h) is an attractive starting point for MRI sensor design, as the protein can be modified to improve stability and alter substrate specificity via directed evolution and rational design approaches. The active site of BM3h possesses a hexacoordinate heme-bound paramagnetic iron center containing a labile axial water molecule[12], allowing the protein to act as an MRI contrast agent. In a recent report, we showed that BM3h demonstrates longitudinal (T_1) ^{1}H MRI contrast enhancement that is modulated by binding of cognate fatty acid ligands in the cavernous active site[13]. A customized high-throughput optical screening method was developed to generate binding isotherms by monitoring P450-Soret absorbance changes as a function of ligand concentration (supplementary fig. 1)[13]. Using directed evolution, we altered ligand specificity to provide BM3h-derived sensors exhibiting high affinity for dopamine (DA). Five rounds of random mutagenesis and screening led to the isolation of variant BM3h-B7, with >300-fold improvement in the dissociation constant (K_d) for DA ($990 \pm 110 \,\mu M$ to $3.3 \pm 0.1 \,\mu M$; table 1, fig. 1b) and an 85% maximal change in the strength of the contrast agent (longitudinal molar relaxivity, r_1, an indicator of MRI contrast agent specific activity given by the slope of the longitudinal relaxation rate $1/T_1$ *vs.* concentration) in response to DA binding. Increases in DA affinity were accompanied by concomitant loss in fatty acid binding; however, screening BM3h-B7 against other important neural markers revealed considerable affinity for similar biogenic amines including norepinephrine (NE) and serotonin (5HT, fig. 1a, 1b).[13] Further improvements in DA specificity will assist application of these sensors in the brain, especially in regions where competing ligands might interfere with DA binding or complicate interpretation of contrast changes produced by the sensors.

We hypothesized that broadly specific sensors such as BM3h-B7 might provide useful starting points for continued directed evolution to generate further improvements in DA selectivity and to create MRI sensors for other neurotransmitters, such as 5HT. The ability to image DA is significant due to the importance of DA in learning, reward, and motor control functions, as well as its role in several neurodegenerative diseases and addiction. 5HT is of interest because abnormalities in 5HT signaling are implicated in depression and other mood disorders. Here we demonstrate that the structural analysis of BM3h variants can guide

directed evolution efforts. Targeting mutations to residues in the active site that directly contribute to ligand binding has allowed us to generate highly selective BM3h MRI sensors. We report DA sensors with improved affinity and ligand specificity, as well as the first reported protein-based MRI sensor for 5HT, which demonstrates excellent specificity combined with sub-micromolar affinity. We also show that mutations to the active site of BM3h result in molecular MRI sensors with enhanced contrast effects and ligand-dependent signal changes. Finally, we provide X-ray crystallographic data that elucidate the basis of BM3h ligand binding, selectivity and T_1 relaxivity changes. This work represents one of the few systematic structural investigations of protein lineages derived from directed evolution and demonstrates at the atomic level how mutations lead to altered ligand binding and MRI contrast.

RESULTS

Structural basis of DA binding in evolved BM3h variants

In wild type and evolved BM3h variants, DA, 5HT and NE show binding behavior marked by a red-shifted Soret band indicative of axial iron coordination by the neurotransmitter (supplementary fig. 1). Structure-activity studies with DA homologues modified at the amine and hydroxyl moieties identified the 2-amino group as responsible for this interaction (supplementary fig. 2a and ref. 12). DA, 5HT and NE likely share similar binding modalities, based on their related structures (fig. 1a) and the broad specificity observed for BM3h-B7 and its progenitor BM3h-8C8 (fig. 1b)**.** We predicted that improvements in selectivity might be achieved with mutations focused to the protein active site. X-ray crystallography was used to obtain the structures of the DA- and 5HT-bound proteins and choose positions for saturation mutagenesis, which accesses amino acid substitutions that are not accessible by random point mutagenesis. Ligand-bound structures were obtained by co-crystallization in the presence of 2 mM DA or 5HT and show active site electron densities that allow for unambiguous assignment of the neurotransmitter (supplementary fig. 3). A full summary of X-ray crystallographic data for BM3h-8C8 and BM3h-B7, as well as other BM3h variants described below, can be found in supplementary tables 1 - 6.

BM3h is composed of two subdomains, an N-terminal beta-domain and an alpha helical-rich subdomain that includes the heme-bound active site (supplementary fig. 4). The active site is enclosed by several alpha helices, including the B'-helix (residues 73-82), I-helix (residues 252-282), active site capping F- and G-helices (residues 172-227), as well as several flexible loops. In the presence of cognate fatty acid substrates, BM3h undergoes ligand-dependent conformational changes, with pronounced movements in the F-, G- and I-helices, that are important for the low-spin to high-spin iron transition and catalysis[19]. Conformational heterogeneity observed among evolved BM3h variants is independent of neurotransmitter binding, suggesting that binding in solution does not induce the same large-scale backbone changes (see supplementary fig. 4 for a detailed discussion).

DA-bound BM3h-8C8 and BM3h-B7 structures (fig. 1c - 1f) confirm axial heme coordination by the DA amine. In both variants, the backbone carbonyl of A330 acts as a bifurcated hydrogen bond acceptor to the catecholic DA hydroxyls (fig. 1c, 1d). DA binding is further stabilized by two networks of water molecules that form bridging hydrogen bonds between the DA *p*-hydroxyl group (fig. 1c, 1f) and BM3h functional groups such as the backbone carbonyl of L437, a heme proprionate, and the backbone amide nitrogen of A74. Comparison of DA-bound structures and published BM3h structures suggests that similar bound water networks are found in the protein active site even in the absence of ligands[20]. Interactions between BM3h and DA hydroxyls and amine are, for the most part, independent of acquired amino acid mutations. These interactions probably contribute to the low but non-negligible DA affinity exhibited by wild type BM3h ($K_d \sim 1$ mM).

BM3h-8C8 and BM3h-B7 share three active site mutations, T268A, I263A, and L75P (fig. 1b). Biochemical evidence suggests that the mutations located outside of the active site do not make significant contributions to DA affinity improvements. Shortening of the T268 side-chain by mutation to alanine may prevent steric clash between the T268 Cγ and DA ethylamine (fig. 1c - 1e). In the wild type protein, the T268 hydroxyl inserts into and bends the P450 I-helix by hydrogen bonding to the backbone carbonyl of A264, disrupting i – i+4 hydrogen bonding. While the I-helix remains bent in T268A variants, we observe a rotation of the I-helix between F261 and A264 (fig. 1e). This rotation may create an unfavorable clash between I263 and F81 that is alleviated in subsequent generations by mutation I263A. It is known that substrate-dependent I-helix rotations are important for enzymatic catalysis,[19] and others have observed similar I-helix rotations after mutating nearby residues such as A264[21].

L75P appears to improve hydrophobic packing of the DA catechol against the side-chain of F87, which sits just above the heme. In wild type BM3h, the orientation of F87 is dictated by the side-chain of L75. In BM3h-8C8, the L75P mutation allows F87 to swing away from the ligand-binding pocket to accommodate the DA catechol in a tilted-T 'π-stacking' interaction (fig. 1d). L75 resides in the B'-helix, yet its mutation in BM3h-8C8 does not significantly alter the protein backbone. However, in daughter variant BM3h-B7, mutation F81L induces large-scale collapse of this helix into the active site (3.7 Å Cα - Cα change at A74, fig. 1f). The comprehensive structural analysis of the BM3h-8C8/BM3h-B7 lineage allows us to pinpoint at what point during evolution such large-scale backbone changes occur. Had we limited X-ray crystallographic efforts to the endpoint BM3h-B7 variant, we would likely have postulated that a helix- destabilizing L75P mutation was sufficient for this movement. F81 packs against I263A, which, as noted above, assumes a slightly rotated conformation due to mutation at T268A (fig. 1e, 1f). We conclude that the displacement of the B'-helix of BM3h-B7 involves the subtle interplay of all 4 mutations. α-Helix movements have been observed in other proteins engineered for ligand binding: evolution of an aminoacyl-tRNA synthetase selective for *p*-bromophenylalanine included a proline-induced α-helix rotation that resulted in significant restructuring of the enzyme active site[24]. B'-helix collapse within BM3h-B7 allows an active site water to form a bridging hydrogen bond between the amide nitrogen of A74 and DA *p*-hydroxyl (fig. 1f), contributing to the ~ 3-fold (0.6 kcal/mol) increase in affinity over BM3h-8C8. Consistent with structure-activity investigations (supplementary fig. 2), while hydrogen bonding to DA hydroxyls provides some improvement in binding (~ 2–5 fold), it appears that the bulk of affinity increases in these mutants results from optimized van der Waals packing resulting from side-chain mutations.

Shared binding determinants contribute to overlapping DA and 5HT specificity in BM3h-8C8

Evolved DA binders BM3h-B7 and BM3h-8C8 also bind 5HT, with K_d values of 18.6 ± 0.1 and 80 ± 8 μM, respectively (fig. 1b **and** table 1). To assess the origin of this overlapping specificity, BM3h-8C8 was co-crystallized with 5HT (fig. 2 **and** supplementary table 1, 6). An overlay of DA- and 5HT-bound BM3h-8C8 shows that 5HT occupies the same active site cavity as DA and shares similar hydrophobic packing to active site side-chains (fig. 2b). The exocyclic 5HT hydroxyl similarly hydrogen bonds to the backbone carbonyl of A330 and active site water networks. The indole nitrogen is oriented in such a way as to allow direct hydrogen bonding to the backbone carbonyl of L437. This interaction may compensate for the loss of hydrogen bonding to the DA *p*-hydroxyl (fig. 1c). Based on these structures, no clear steric or hydrogen-bonding character substantially distinguishes either ligand; the similar binding configuration observed for DA and 5HT accounts for the relatively low specificity displayed by BM3h-B7 and -8C8.

Active site directed evolution yields 5HT-selective BM3h variants

Based on the crystal structures of the DA- and 5HT-bound proteins and using BM3h-B7 as the parent scaffold, we designed libraries in which mutations were focused around both faces of the neurotransmitter aromatic ring. Each library consisted of saturation mutagenesis at two positions to maximize diversity (1024 possible nucleotide sequences) yet maintain a reasonable size for optical high-throughput titrations. Each library included site-saturation at F87, which lies directly above the BM3h heme (fig 2) and has been shown to be important for altering substrate specificity in evolved BM3h monooxygenases[25]. Three 2-site libraries were constructed: F87+A74, F87+L75 and F87+T438 (fig. 2b). A74 and L75 (L75P in BM3h-B7) are located in the B'-helix, and T438 is located in an adjacent loop. Screening was performed as in our earlier work[13], with slight modifications (supplementary Fig. 1d). Briefly, libraries were transformed into *E. coli* and ~ 900 distinct colonies were expressed in 96-well blocks. Clarified lysate was distributed among three 96-well microtitre plates to allow simultaneous positive/negative screening against DA, 5HT and NE. Variants demonstrating improved binding or altered selectivity were isolated, purified to homogeneity and analyzed for binding and ligand-dependent MRI activity.

No improvements in DA affinity or selectivity were acquired by these mutants. However, a variety of BM3h variants were obtained with altered selectivity favoring 5HT. Clear trends in 5HT binding affinity were observed at F87 with preference for aliphatic hydrophobic amino acids (L is preferred, followed by V, A, and G; supplementary Fig. 5a). A single mutation, F87L (this variant is denoted BM3h-3AE4; fig. 1b **and** table 1), was sufficient to induce preference for 5HT (K_d of 3.9 ± 0.1 μM, a ~ 5-fold improvement compared to BM3h-B7), with approximately 6-fold selectivity over DA (21.4 ± 1.3 μM) and 30-fold over NE (91.3 ± 0.2 μM). A second mutation, T438L, further improved 5HT binding when combined with F87L. Denoted BM3h-3DB10 (fig. 1b **and** table 1), this variant bound 5HT with a K_d of 1.1 ± 0.2 μM and was ~ 45-fold selective with respect to DA and 190-fold with respect to NE.

We next investigated whether 5HT-specific BM3h-3DB10 demonstrated ligand-dependent relaxivity (r_1) changes. Unfortunately, while BM3h-3DB10 exhibited 5HT-dependent decreases in r_1 (table 1), relaxivity observed in the absence of ligand (0.73 ± 0.05 mM^{-1} s^{-1}) was substantially less than wild type BM3h (1.23 ± 0.07 mM^{-1} s^{-1}), limiting the overall MRI signal change achievable by this sensor. The ligand-free Soret band of BM3h-3DB10 is red-shifted from 419 nm to 422 nm (supplementary fig. 5b). This shift may reflect changes in the local heme environment or even partial coordination of the heme iron by nearby amino acids. Similar effects have been observed in BM3h mutants that introduce metal-coordinating amino acids near the heme[20]. Iron coordination by residues within the active site would compete with water occupancy at the heme, reducing r_1.

Since wild type BM3h shows higher r_1 than BM3h-3DB10, we asked whether 5HT-selective mutations could restore affinity in the wild type background ($K_d > 2.5$ mM, table 1). Mutation F87L produces a variant, BM3h-L4, with a K_d of 199 ± 1 μM (fig. 3a **and** table 1), augmenting 5HT binding ~ 13.5-fold. The subsequent addition of T438L (variant BM3h-L6) further improves binding to 9.3 ± 1.3 μM. The increase in 5HT binding affinity contributed by these two mutations is similar in scale to DA affinity enhancements achieved by eight mutations in BM3h-B7. Moreover, BM3h-L6 is 80-fold selective over DA ($K_d > 750$ μM) and shows no binding to NE. Binding improvements due to T438L require F87L, as the T438L single mutant, BM3h-L5, demonstrates no significant 5HT binding (table 1). Relaxivities measured for BM3h-L4 and BM3h-L6 in the absence of ligand ($r = 1.55 \pm 0.14$ mM^{-1}s^{-1} and 1.44 ± 0.13 mM^{-1}s^{-1}, respectively, table 1) were greater than that of wild type BM3h. These variants maintained ligand-sensitive relaxivity decreases of ~30% and ~78%, respectively, upon addition of 2 mM 5HT.

Cumulative improvements in BM3h-L6 5HT affinity suggested that binding could be further enhanced by saturation mutagenesis at additional active site locations. Iterative saturation mutagenesis has been used to improve enzyme activity on new substrates[26] and enantioselectivity[27] by directed evolution. The small diversity (n = 32) of single-site libraries is easily covered in one 96-well plate, and many single-site saturation libraries can be screened in a couple of days. Six additional sites, L75, I263 and T268 (mutated in BM3h-B7) as well as A74, A328, and L437 were chosen based on proximity to the bound ligand (see fig. 1 **and** 2). From this, variant BM3h-2G9, mutated at T268S, was isolated (5HT – K_d - = 3.3 ± 0.2 μM, fig. 3a). Subsequent saturation mutagenesis at remaining sites produced BM3h-2G9C6 (F87L, T438L, T268S, L437Q) with sub-micromolar affinity for 5HT (K_d = 0.7 ± 0.2 μM) and > 250-fold selectivity over DA and NE (K_d = 198 ± 7 μM and K_d = 275 ± 40 μM, respectively, fig. 3a **and** table 1). BM3h-2G9C6 maintains 5HT-dependent decreases in MRI contrast and exhibits the highest ligand-free r_1 (1.89 ± 0.02 mM^{-1}s^{-1}) of any ferric P450-based MRI contrast agent we examined (table 1). 2G9C6 contains an additional mutation, R51C, probably the result of polymerase error during library construction. Reversion of this mutation had little impact on binding and relaxivity. It is notable that 4 mutations within the active site improve 5HT binding by ~ 4000-fold without negatively affecting T_1 relaxation enhancement; indeed, the relaxivity is enhanced. Moreover, unlike the more distributed mutations accumulated in BM3h-B7, the accumulated active site mutations have minimal impact on protein stability (table 1 and **supplementary methods**), which will facilitate further engineering[7] and *in vivo* applications.

BM3h-based sensors detect serotonin release in cell culture

Screening BM3h libraries in lysate permits affinity selection in the context of potential competitors derived from bacterial metabolism. However, *in vivo* application requires that sensors be robust, sensitive, and specific in mammalian extracellular environments. To demonstrate the utility of the evolved sensor to detect biologically-stimulated 5HT release, we chose rat basophilic leukemia RBL-2H3 cells, a canonical model cell line for studying Ca^{2+}-mediated and ligand-stimulated 5HT secretion from cultured cells (fig. 4a). Long thought to model some features of mucosal mast cell responses to stimuli, RBL-2H3 cells have been previously used for direct imaging of 5HT fluorescence in secretory granules by multiphoton microscopy, in a manner allowing quantification of intragranular 5HT concentration.[30] 50 μM BM3h-2G9C6 protein exhibited a 9.7 ± 0.3% decrease in longitudinal relaxation rate (R_1) in cell supernatant extracted 15 min after stimulation with 2.5 μM ionomycin. Wild type BM3h showed negligible (0.9 ± 0.6%) change in R_1 under these same conditions. Using a ligand depleting binding model, we estimated that observed BM3h-2G9C6 R_1 changes correspond to a 5HT concentration of approximately 31.0 ± 1.0 μM in supernatants of ionomycin-treated cells, which corresponds well to estimates obtained from measurements using a commercial colorimetric 5HT ELISA assay (fig. 4b).

Specificity of BM3h-2G9C6 for binding 5HT was further assessed by examining responses to common 5HT precursors and metabolites (supplementary fig. 2b). Amino acid precursors tryptophan and 5-hydroxytryptophan demonstrate no observable binding when incubated with BM3h-2G9C6. Specificity is also observed against the monoamine oxidase-catalyzed 5HT degradation product 5-hydroxyindoleacetic acid as well as melatonin, a 5HT derivative important for regulating circadian processes and found in high concentrations in the pineal gland[31]. These data suggest that BM3h-2G9C6 will be useful for selective 5HT visualization in biological settings.

Binding determinants in evolved BM3h 5HT sensors

Crystal structures of 5HT-selective variants BM3h-2G9 and BM3h-2G9C6 were determined in order to help understand the origins of the observed binding specificity and MRI contrast

effects (figure 3c - 3f). As in BM3h-8C8, the 5HT amine coordinates the heme iron; however, 5HT does not interact with the backbone carbonyl of A330. Instead, 5HT occupies a different orientation with the hydroxyindole group pointing towards the L437Q/T438L loop (figure 3f). This alternate conformation is favored following introduction of two leucine mutations, F87L and T438L, which also provide significantly improved 5HT affinity (from > 2 mM in wild type BM3h to < 10 μM in BM3h-L6). As shown in figure 3c, these side chains pack against each face of the 5HT aromatic ring system. Subsequent deletion of the Cγ-methyl in T268S accommodates the 5HT ethylamine (fig. 3c and 3d). This mutation parallels T268A in evolved DA variants. Hydrophilic 5HT functionalities form hydrogen bonds to existing BM3h water networks that are often observed in the absence of ligand.[20] In BM3h-2G9, for example, one water molecule bridges the indole nitrogen of 5HT and the propionic acid side-chain of the heme cofactor. The exocyclic 5HT hydroxyl interacts with a water network that splits the I-helix as well as interacts with the side-chain hydroxyl of T268S (fig. 3d). Alanine was enriched at this location in earlier variants such as BM3h-8C8. As the DA catechol occupies a different orientation in the BM3h active site (fig. 1c), there was no selective advantage to maintain the side chain hydroxyl at position 268 during evolution experiments for improved DA affinity.

The addition of L437Q in BM3h-2G9C6 improves binding to $K_d \sim 700$ nM (table 1). As shown in figure 3e, the 5HT ring in BM3h-2G9C6 is rotated compared to BM3h-2G9, possibly due to an alternative water network bridging the exocyclic hydroxyl and side-chain of L437Q. The L437Q amide adopts an orientation that also promotes a dipole-dipole interaction with the hydroxyindole ring. Improved hydrophobic packing and flexible hydrogen bonding to various water networks may contribute significantly to 5HT binding enhancements attributed to this mutation.

One striking feature of BM3h-2G9 and BM3h-2G9C6 is their remarkable selectivity for 5HT over DA and NE. Whereas BM3h-8C8 and BM3h-B7 have K_d values within an order of magnitude for all three ligands, BM3h-2G9C6, for example, demonstrates > 250-fold preference for 5HT over DA. As discussed above, broad specificity in BM3h-8C8 likely results from shared binding determinants exploited by both DA and 5HT. In 5HT-specific variants, the ligand occupies an alternate active site pocket (fig. 3f, see discussion). Our attempts to isolate DA-bound BM3h-2G9C6 crystals were unsuccessful, but simple modeling suggests that the DA ligand is too short to allow proper packing against T438L or to form hydrogen bonds to water molecules exploited by 5HT (data not shown). In addition, the lack of the indole nitrogen prevents DA hydrogen bonding to the propionic acid water network as observed for 5HT.

Improved DA sensors by active site mutagenesis

Based on the success of 5HT sensor evolution, we asked whether active site-directed saturation mutagenesis could also generate improved BM3h-derived DA sensors. Nine active site residues in wild type BM3h were chosen for randomization: I263, A264, E267, T268, T327, A328, T436, L437 and T438. As shown in fig. 3b and table 1, accumulating single mutations (T268A, I263A, T438V and A328G) yielded a new variant, denoted BM3h-9D7, with improved affinity ($K_d = 1.3 \pm 0.1$ μM), ligand selectivity (5HT K = 70 ± 3 μM and NE K = 37 ± 1 μM) and relaxivity (1.31 ± 0.07 mM^{-1}S^{-1}) compared to BM3h-B7 and wild type BM3h.

In DA-bound BM3h-9D7 (fig. 5), the DA catechol ring is oriented towards the same active site cavity as in BM3h-8C8 and BM3h-B7 (fig. 1). The ability of 5HT to share this binding modality (fig. 2) may account for BM3h-9D7's weaker ability to discriminate among various neurotransmitters when compared to highly selective variants such as BM3h-2G9C6. Nevertheless, the > 50 fold preference for DA over 5HT in BM3h-9D7,

resulting from mutations in the ligand binding pocket, marks a substantial improvement in selectivity when compared to BM3h-B7, which demonstrates only a ~ 5 fold preference for DA over 5HT. This improvement in selectivity should translate well to *in vivo* imaging experiments, where submicromolar concentrations of 5HT are typical.[32]

The BM3h-9D7 structure shows a different solution to DA-catechol binding than found in BM3h-8C8 (fig. 5). In BM3h-9D7, wild type L75 is maintained; as such, the orientation of F87 in the active site overlays well with the wild type protein (fig 5a). However, the side-chain of A328, which packs against the opposite face of the DA catechol, is deleted by mutation to glycine, allowing DA to rotate away from F87. An additional mutation in BM3h-9D7, T437V, in close proximity to A328G, likely improves hydrophobic packing in this region. Differences in catechol orientation may account for the 9-fold difference in DA affinity between these two BM3h variants (fig 5b). In BM3h-9D7, DA takes on a more favorable tilted-T (face-side) 'π-stacking' interaction with the phenyl ring of F87. Rotation of the DA ring may also improve the co-planarity of catechol hydroxyls and A328 backbone carbonyl. As no difference in hydrogen bonding is observed, the increases in BM3h-9D7 binding compared to BM3h-B7 and BM3h-8C8 likely result from improved van der Waals interactions around the DA catechol ring.

Two active site mutations, T268A and I263A, were conserved in all DA-specific variants. This observation led us to investigate whether any enhancements to ligand binding affinity were conferred by the mutations outside of the active site in BM3h-B7 and -8C8.[13] Each round of mutagenesis and screening in the original BM3h-8C8 lineage identified at least one active site mutation (fig. 1b) along with other mutations, not in the active site. Reverting non-active site mutations in BM3h-8C8 (denoted BM3h-L75P) resulted in little change in binding affinity and selectivity relative to the parent (table 1), underscoring the key role of the active site mutations in enhanced neurotransmitter binding. As with BM3h-2G9C6 and BM3h-9D7, however, the r_1 of BM3h-L75P (1.64 ± 0.02 mM^{-1}s^{-1}) was substantially improved by limiting mutations to the active site.

Structural insights into BM3h MRI relaxivity differences

Although 5HT- and DA-selective BM3h variants were not isolated on the basis of MRI contrast properties, they exhibited substantially different relaxivities that corresponded to trends in structural factors we identified by crystallography of BM3h sensor lineages. Key determinants of r_1 include solvent access to the heme, the geometry of the heme water coordination (chiefly r, the iron-water proton distance), the exchange rate of bound water molecules (T_M), and the electronic relaxation time of the heme iron atom (T_S). Two structural features suggested that increased water access might help explain the improved relaxivity of some of the mutant proteins. First, structures for unliganded forms of BM3h-8C8, 2G9, 9D7, and 2G9C6 ($r = 1.1, 1.27, 1.31,$ and 1.89 mM^{-1}s^{-1}, respectively) showed regions of amorphous electron density near the heme (Supplementary fig. 6c - 6g), possibly reflecting heme-associated water molecules[20]. These regions were larger for variants with higher relaxivity. Second, we found evidence that higher r_1 variants demonstrate increased flexibility within certain regions of the active site, perhaps facilitating exchange of water molecules into and out of the site. In BM3h-2G9C6, L437Q, E264, and H266, show alternate conformations among crystallographic monomers that are not observed in low-relaxivity variants (Supplementary fig. 7a - c); trends in increasing B-factor at these locations are also observed (Supplementary fig. 7d - f). One region, the loop at the top of the active site, contains both L437Q and T438L mutations found in BM3h-2G9C6 (Supplementary fig. 7i,j). Interestingly, this loop also flanks two of the three main channels that allow water access to the BM3h active site and the side chain of L437Q is observed to hydrogen bond to waters in these channels (fig 3e).

To obtain additional information about structural determinants of BM3h relaxivity, we measured the r_1 of evolved variants as a function of proton NMR frequency from 0.01 – 42 MHz (Supplementary fig. 8), to obtain so-called nuclear magnetic relaxation dispersion (NMRD) curves. Among the set of BM3h variants analyzed, r_1 differences measured by MRI at 200 MHz were more pronounced at lower field, and displayed sigmoidal transitions (dispersions) at proton NMR frequencies of roughly 0.5 MHz. After correcting for a modeled diamagnetic contribution[33], NMRD data were well fit (R^2 = 0.997 across mutants) to a dipolar relaxation model consisting of a single inner sphere water (q = 1) and a single low-spin iron (S = 1/2), with r, T_M, and a field-independent T_S as free parameters (Supplementary fig 8, **Inset**). Estimates of r ranged from 2.6 – 3.0 Å, in good agreement with high field NMR[36] and EPR[37] studies of P450 enzymes. Variations in T_M (0.05 – 5 μs, with shorter values corresponding to higher r_1) and T_S (0.5 – 0.8 ns) across mutants were necessary to explain differences in the dispersion frequencies and asymptotic r_1 values. Although the T_M values are probably only valid as order-of-magnitude estimates, the observed trend is consistent with structural evidence that parameters affecting exchange of bound waters might be particularly important for relaxivity changes in BM3h variants. The NMRD results also suggest that orientation of bound water molecules (reflected by r) is important for determining relaxivity, but the crystal structures do not have high enough resolution to confirm or refute this possibility.

There was spectroscopic evidence that the BM3h variant with the lowest observed relaxivity, BM3h-3DB10 (r_1 = 0.73 mM^{-1}s^{-1}), experienced a decrease in the minor population of S = 5/2 iron atoms observed in most P450 variants[38]. Other variants showed virtually identical spectra to wild type BM3h (Supplementary fig. 6b), however, and the relatively subtle changes in T_S required for NMRD model fitting suggests that differences in electronic relaxation properties are not very important for relaxivity determination among protein variants. Collectively, the data argue that relaxivity enhancements in BM3h variants are accessible by protein engineering, and that alterations to solvent interaction parameters may be the primary mechanism by which mutations affect r_1.

Discussion

We have shown that structure-guided iterative site-saturation mutagenesis within the active site of P450 BM3h can significantly improve its performance as a ligand-responsive MRI contrast agent. A few active site mutations dramatically increased DA and 5HT affinity to levels within range of the physiological concentrations of these molecules in the brain. For example, four mutations in BM3h-2G9C6 were sufficient to achieve submicromolar K_d values for 5HT, representing an average affinity improvement of 10-fold for each mutation. This sensor was capable of detecting 5HT release from mammalian cells in culture, and 5HT concentration estimates obtained by MRI compared well with an MRI-independent 5HT ELISA assay. It has been reported that deep brain stimulation can evoke the release of 5HT in the dorsal raphe nucleus at concentrations approaching 1 μM.[32] The binding affinity of BM3h-2G9C6 (K_d ~700 nM) is suitable to detect 5HT under these conditions. In addition, the high selectivity of BM3h-2G9C6 should minimize confounding signal changes due to local concentrations of DA, which have repeatedly been shown to approach 10 μM in the ventral striatum. On the other hand, the improved DA binding of BM3h-9D7 makes it well suited for observing these levels of DA in the brain.[39] We expect similar evolutionary strategies can be applied for the production of BM3h-based sensors for a variety of biologically important molecules.

The ability of BM3h to adapt to amphipathic ligands such DA and 5HT with only a few active site mutations is impressive, especially bearing in mind that the cognate substrates of the parent enzyme are long-chain aliphatic fatty acids. Important insights into the molecular

origins of improved ligand binding, with respect to these neurotransmitters, are provided by careful analysis of crystal structures of a panel of ligand-bound BM3h variants. Amino acid side-chain mutations almost exclusively improve hydrophobic packing against the aromatic rings and ethylamine portions of bound DA and 5HT. On the other hand, exocyclic hydroxyls and the 5HT indole nitrogen make use of backbone amides and active site water molecules to form stabilizing hydrogen bonds. Improvements in these interactions by directed evolution are marked by adjustments in hydrogen bonding networks rather than the introduction of side chains that directly hydrogen bond to the ligand. Computational design approaches that attempt to engineer side chain:ligand hydrogen bonds face an uphill battle due to strict geometric requirements and limited sampling[40]. Evolution has arrived at an elegant alternative solution by exploiting flexibility in water networks to accommodate hydrophilic functionality in non-polar pockets. In addition, by making use of existing protein-bound water networks rather than recruiting new ones, the energetic cost associated with water rearrangement is likely very low[41]. Computational approaches that take water into consideration may lead to considerable improvements in design.

While earlier BM3h evolution experiments using random mutagenesis and screening led to significant enhancements in DA affinity, the resulting sensors demonstrated broad specificity for structurally similar neurotransmitters including 5HT and NE[13]. Nonetheless, these non-specific sensors offered important starting points for further evolution. By focusing mutations to the ligand-binding pocket, we were able to isolate DA- and 5HT-specific variants that showed marked selectivity relative to similar biogenic amines. For example, BM3h-9D7 demonstrates a ~ 10 fold improvement in selectivity over 5HT when compared to BM3h-B7. Tuning the local active site environment with the A328G mutation provides an alternative hydrophobic packing solution that improves binding to the DA catechol functionality while at the same time creating a less favorable setting for 5HT recognition, which can occur at the same active site cavity (figure 2 and 5). The crystal structures of highly specific 5HT sensors show an alternative conformation of the 5HT ring with respect to more broadly specific DA- and 5HT-binding BM3h variants. By using detailed structural information from a set of 5HT and DA-bound BM3h lineages, we are able to pinpoint locations within the active site that are important for maintaining or altering ligand binding geometry. Isolating active site mutations that favor alternative selective binding geometries over orientations that can be shared by similar ligands may be a general means to obtain highly selective sensors. Similar promiscuous protein function has been suggested to be important in natural protein evolution, where basal levels of promiscuous function (catalysis, substrate specificity etc.) that provide even a minimal advantage under selective pressures may provide starting points for the evolution of completely new protein function[44]. The evolution experiments for 5HT selectivity described here mimic this process in a laboratory setting. However, by applying a structure-guided saturation mutagenesis approach in the active site of BM3h, we are able to arrive at these solutions more rapidly than through random mutagenesis.

We observe considerable improvements in other properties including thermostability and T_1 relaxivity in the active site mutants, whereas continued random mutagenesis often led to deterioration in MRI contrast induction. Random mutagenesis and screening more accurately reflects natural protein evolution processes and arrives at similar binding solutions to active site mutagenesis. However, additional accumulating mutations, while neutral with respect to ligand binding, may prove detrimental to MRI sensor sensitivity. Many of the sensors described here show enhanced longitudinal relaxivity, signifying that MRI signal is a function of the protein sequence and therefore can be improved by evolution. Indirect structural information provided by X-ray crystallography of a series of BM3h variants suggests that increased flexibility in certain regions of BM3h that enhances water access to the protein active site may contribute to these improvements. These results

are supported by NMRD experiments that show that changes in water residence time at the heme iron center correlate with differences in relaxivity properties. We have recently shown that > 2.5-fold improvements in MRI signal can be obtained by swapping the ferric heme center with a non-natural Mn^{3+}-containing porphyrin[45]. We expect that combining such alternative protein engineering strategies with contrast-enhancing directed evolution will generate novel BM3h-derived MRI sensors with the potential to rival organometallic chelates.

Material and Methods

Materials

Dopamine hydrochloride, neurotransmitter homologues, lysozyme, DNase, δ-amino levulinic acid (δ-ALA) and buffers were purchased from Sigma-Aldrich. Serotonin hydrochloride was from TCI America, and norepinephrine bitartrate was from ChemPacific. Growth media such as Terrific Broth (TB) and Luria Broth (LB) were purchased from Research Products International. Restriction enzymes and other enzymes used for cloning were obtained from New England BioLabs. Oligonucleotide primers were from Integrated DNA Technologies.

P450 general cloning and library construction

P450-BM3h variants were cloned into and expressed from a modified version of plasmid pCWori, a derivative of plasmid pHSe-5. This vector contains an ampicillin resisitance marker for plasmid maintenance, a pBR322 origin for plasmid replication and a constitutively expressed copy of the lac repressor; IPTG inducible expression is controlled by a *lacUV5* promoter and two tandem copies of the *tac* promoter. PCR-amplified P450 gene products are generally cloned between 5′ BamHI and 3′ EcoRI restriction sites. To facilitate protein purification, a terminal 6XHis coding sequence was engineered into pCWori, just prior to the stop codon and EcoRI restriction site. An XhoI site was introduced prior to the 6XHis sequence to permit cloning of His-tagged P450 BM3h variants.

P450 site-directed mutagenesis and site-saturation library construction was achieved by assembling PCR fragments made from oligonucleotides containing the desired codon mutation or a degenerate NNK (or for reverse primers, the reverse complement MNN; where N = A,T,G,C, K = G,T and M = A,C) codon, which codes for all 20 amino acids and the TAG stop codon. PCR fragments were assembled using either standard overlap extension PCR or through restriction cloning using the Type IIS restriction enzyme, BsaI, depending on convenience. For example, if two mutation sites were located close together in the BM3h sequence, scarless restriction cloning with BsaI, which allows for tailored overhang regions for ligation, proved preferable to overlap extension PCR[48]. In general, both methods prove equally efficient for site-directed mutagenesis and library construction. A detailed list of primers will be made available upon request.

P450 expression and purification

For expression, pCWori-cloned P450-BM3h variants were transformed into *E. coli* strain BL21(DE3) and expression pre-cultures were grown up, overnight, at 37 °C in LB supplemented with 100 μg/mL of ampicillin. 5 mL pre-cultures were used to inoculate 500 mL of TB medium supplemented with ampicillin. An iron-rich heavy metal supplement (1000X = 50 mM $FeCl_3$, 20 mM $CaCl_2$, 10 mM $MnSO_4$, 10 mM $ZnSO_4$, 2 mM $CoSO_4$, 2 mM $CuCl_2$, 2 mM $NiCl_2$, 2 mM Na_2MoO_4, and 2 mM H_3BO_3) and 500 μM δ-ALA, a heme biosynthetic precursor, were also added to media to improve protein yields. Expression cultures were grown to mid-log phase (A_{600} ~ 0.5), with constant shaking, at 37 °C and subsequently allowed to drop to room temperature before induction with IPTG at a final

concentration of 500 μM. Protein expression was carried out for 16 hours at room temperature before harvesting.

Expression cultures were harvested at 6,000 × g for 10 minutes in a Beckman Coulter Avanti J-25 centrifuge. Cell pellets were resuspended in 25 mL of buffer (25 mM Tris pH 8.0, 300 mM NaCl, 20 mM imidazole) supplemented with 0.5 mg/mL of hen egg white lysozyme. Cells were incubated on ice for one hour before lysis by sonication. Clarified lysate was loaded onto a HisTrap™ HP 5 mL Ni-NTA column (GE Healthcare) and, after washing with low imidazole buffer, 6XHis-tagged P450 was eluted by increasing the imidazole concentration to 165 mM. 6XHis purified protein was buffer-exchanged into 20 mM Tris, pH 8.0, by consecutive washing in an Amicon® Ultra centrifugal filter (Millipore) to remove salt and imidazole. The protein was then further purified by anion exchange over a HiTrap™ 5 mL Q HP column (GE Healthcare) and eluted by the gradient addition of 0 mM – 450 mM NaCl. Protein typically came off the column at ~ 250 mM NaCl. Purified protein was exchanged into phosphate-buffered saline, flash frozen on dry ice and stored at − 80 °C until needed. Proteins intended for crystallography were exchanged into low salt tris buffer (20 mM tris, pH 8.0, 20 mM NaCl) over a Sephacryl™ 200 high-resolution size exclusion column (GE Healthcare) prior to setting up crystal trays.

Preparing P450-BM3h library variants for high-throughput screening

Individual colonies from BM3h variant libraries were picked into 96-well expression blocks containing 400 μL LB supplemented with ampicillin. Typically, 4 – 8 wells of each block were reserved for control plasmids expressing BM3h variants with known neurotransmitter affinities. These pre-cultures were allowed to grow to saturation, overnight at 37 °C. The following day, using a Beckman MultiMek™ 96 automated liquid handling robot, 100 μL of each pre-culture was transferred to a 96-well plate containing 100 μL of 50% glycerol for storage at −80 °C for subsequent plasmid isolation and sequence interrogation. An additional 100 μL of culture was inoculated into 1 mL of TB medium supplemented with ampicillin and heavy metal supplement. For high-throughput lysate experiments, δ-ALA was not provided to the cells due to an observed high background absorbance resulting from excessive amounts of free heme in the lysates. Expression cultures were grown for 3 hours at 37 °C prior to induction with 500 μM IPTG and overnight expression at room temperature.

After overnight expression, cells were harvested at 3500 × g for 10 minutes. The medium supernatant was discarded and cell pellets were subjected to 1 round of freeze-thawing at − 80 °C to facilitate cell lysis. Thawed cell pellets were resuspended in 1 mL of PBS supplemented with 0.5 mg/mL hen egg white lysozme and 0.03 mg/mL DNase and incubated at 37 °C for 2 hours. After lysis, cell debris was pelleted at 4500 × g for 15 minutes. 200 μL of clarified lysate was transferred to each of three 96-well microtiter plates using an automated liquid handling robot. Individual plates were screened against DA, 5HT or NE, respectively, (see below).

Neurotransmitter binding affinities

Prior to titration experiments, purified P450 concentrations were measured using a standard CO binding assay. Neurotransmitter binding was monitored by differential absorbance spectroscopy of the heme Soret band in the presence of ligand. Absorbance measurements were taken at room temperature using a Tecan Infinite® M200 absorbance plate reader. Prior to each experiment, protein and ligands were stored on ice in the dark. In a typical experiment, 20 μL of a 10 fold concentrated ligand solution, in degassed PBS, was added to 180 μL of protein (~ 2 – 3 μM in PBS). Absorbance spectra were collected from 350 nm to 500 nM and the difference absorbance spectra at various ligand concentrations were

obtained by subtracting absorbance scans in absence of ligand (i.e. substituting 20 µL of PBS for ligand stock solution). Binding isotherms were generated by measuring the total change in absorbance between the maxima (435 nm) and minima (415 nm) of each difference absorbance spectra (δA_{435nm} - δA_{415nm}) at each ligand concentration. An example of data obtained from these measurements is provided in supplementary fig. 1. The apparent dissociation constant, K_d, the extrapolated maximal absorbance change, A_{max}, and absorbance baseline, A_0, were estimated by fitting binding isotherms to a non-linear ligand depleting binding model, equation (1), using Matlab © (2011, The Mathworks, Inc.)

$$\Delta Abs_{(435nm-415nm)}=A_0+A_{max}\left([P_T]+[S_T]+K_d\right)-\frac{\sqrt{([P_T]+[S_T]+K_d)^2-4[P_T][S_T]}}{2[P_T]} \quad (1)$$

[P_T] gives the total protein concentration and [S_T] indicates the total added substrate concentration.

High-throughput ligand titration experiments

For each series of titrations, 12 concentrated ligand stocks were prepared in degassed-PBS and stored on ice. Typically, 3-fold serial dilutions, centered on the neurotransmitter K_D for the parent P450-BM3h variant, were found sufficient to span a generous range of ligand concentrations, allowing sub-saturation, mid-point and saturation events to be observed. For titrations, zero point measurements were taken, scanning 305 - 505 nm, in the absence of ligand. Subsequently, 10 µL of the lowest concentrated ligand stock solution was added to each well and the absorbance was measured again from 305 - 505 nm. This process was repeated, iteratively, for each of the twelve serial stock solutions. This process was performed for each of three duplicate plates to allow the co-screening of DA, 5HT and NE, independently, for each protein variant.

The final concentration of protein in solution is decreased 1.6 fold by the addition of 12 portions of ligand; however, control experiments demonstrated that this small dilution of protein in high-throughput screening does not significantly alter measured K_D values. Varying protein concentration from 0.5 µM to 5 µM produces results in less than 10% changes in apparent K_D. In general, we have noticed that K_D values measured using this methodology, in lysate, are consistently about 3-fold higher than those determined on the same purified protein. This difference in ligand binding may be due to sequestration of the ligand by components of the cellular milieu or by competition with other cellular factors.

To facilitate data analysis, a MATLAB script was developed for automated data processing and fitting. This program baselines initial Soret band absorbance, generates difference spectra for each ligand concentration along the titration series, calculates the absolute maxima – minima for each difference spectrum, plots binding isotherms for each protein in the 96-well plate, fits these data to a non-linear ligand depleting binding model (similar to equation (1)) and prints goodness of fit statistics for each binding isotherm. The binding model was slightly adjusted to compensate for the small changes in protein concentration that occur upon each subsequent addition of ligand. It was found that the overall dilution factor, under these conditions, scaled with substrate concentration such that:

$$dilution=0.83 \times [S_T]^{-0.035} \quad (2)$$

Therefore adjusting for changes in protein concentration, equation (1) can be modified by multiplying each [P_T] quantity by this dilution factor. The MATLAB script used for these experiments is freely available upon request and should prove useful for others looking to automate similar high-throughput titration experiments.

Depending on the desired screening outcome, those variants that displayed 2-fold or greater improvements in binding for one neurotransmitter (e.g. 5HT) with concomitant increases in selectivity against other molecules (e.g. NE and DA) were rescreened in replicate. The best hits from each round of mutagenesis and screening were the expressed and purified as described and analyzed for accurate binding statistics as well as MRI activity.

Protein Crystallization

Several P450-BM3h variants described in this work were crystallized by vapor diffusion. A 1:1 mixture of a 15 mg/mL protein stock in 20 mM Tris, pH 8.0, and mother liquor was combined in 24-well sitting-drop plates (Hampton Research). Mother liquor compositions depended on the protein variant and are provided in Supplementary table 6. Protein crystals were grown in the absence or presence of ligand. In the ligand-bound conditions, DA or 5HT hydrochloride salts were dissolved at 100 mM concentrations in the presence of a two-fold excess of ascorbic acid as a reductant to prevent oxidation of the ligand during crystallization. A 1/50 fold dilution of neurotransmitter (2 mM final concentration) was added to concentrated protein stocks just prior to setting up each crystal tray. In the absence of reductant, protein crystals and solutions would turn a dark brown color over a period of days indicating oxidation of the neurotransmitter. In the presence of reductant, crystallization trays could be stored, in the dark, for over a period of weeks without any visible substrate oxidation. Under most conditions, crystal growth occurs over the period of 5 – 7 days; however, growth times were significantly shorten by microseeding with shards taken from these crystals. In addition, crystals grown under microseeding conditions grew larger and diffracted with improved resolution.

X-ray data collection and protein structure determination

X-ray diffraction data was collected at the Stanford Synchotron Radiation Lightsource, beamline 12-2 on a Dectris Pilatus 6M detector. Data were collected at 100K and wavelengths for data collection are listed in Supplementary Table 1-5. Diffraction datasets were integrated with XDS[53] and scaled using SCALA[54]. Initial phases were determined using molecular replacement against the wild type P450-BM3h structure taken from PDB 2IJ2, chain A[20]. When more than one structure of the same BM3h variant was solved (i.e. in the presence or absence of ligand), models from one structured were used as molecular replacement for sister structures. In these cases R_{free} statistics were maintained from model to model to prevent over-fitting of the X-ray data (see Supplementary Table 6). Molecular replacement was accomplished using MOLREP software[55], a component of the CCP4 crystallography software suite[56]. Refinement was accomplished with iterative cycles of manual model building within COOT[57] and automated refinement using REFMAC[58] within CCP4. Final cycles of REFMAC refinement included TLS parameters. Non-crystallographic symmetry constraints were not utilized during refinement. Kicked omit maps were generated using the 'calculate maps' feature of the PHENIX software suite for automated structure determination[59]. Statistics for data collection and final protein structure models are given in Supplementary Tables 1 - 5. Model quality was assessed using the 'complete validation' tool included in the PHENIX software suite. Ramachandran outlier statistics, generated from this analysis, can be found in Supplementary Table 6. Ramachandran outliers typically constituted < 0.2 % of all residues, with favored Ramachandran representing > 96.6 % of all residues. Outliers generally lie in a poorly structured loop connecting the P450-BM3 F and G helices (residues 190 – 195). These residues are often missing or marked by poor density in these and other P450-BM3 structures within the protein database. All protein structure figures were generated using PyMol software (The PyMOL Molecular Graphics System, Version 1.3, Schrödinger, LLC.).

MRI longitudinal molar relaxivity measurements

Longitudinal molar relaxivity, r_1, measurements of purified BM3h proteins were performed as previously described with slight modifications. Briefly, 50 μL purified protein samples in a linear range of concentrations were freshly prepared in PBS pH 7.4 with or without 1 – 2 mM 5HT. The samples were imaged in 384-well microtiter plate wells at ambient temperature (23 °C) in a 4.7 T Bruker Avance MRI scanner with a 40 cm bore. T_1-weighted spin echo pulse sequences ($TE = 10$ ms, $TR = 73 – 5000$ ms with increasing averaging with decreasing TR) were used to acquire a 2-mm slice through the each plate. Longitudinal relaxation rates (R_1) were fit to a single exponential from reconstructed image data using custom routines implemented in Matlab (Mathworks).

Cell culture serotonin release assay

Adherent RBL-2H3 rat basophilic leukemia cells (ATCC CRL-2256) were grown in Eagle's Minimal Essential Medium (Lonza) supplemented with 15% (v/v) fetal bovine serum (Invitrogen), 100 U/mL penicillin and 100 μg/mL streptomycin to 80 – 90% confluency in 75 cm^2 flasks at 37 °C, 5% CO_2. The cells were then incubated in complete medium with freshly prepared 5HT at 0.25 mM for 6 hours. The flask was washed three times with 10 mL Locke's buffer (154 mM NaCl, 5.6 mM KCl, 3.6 mM $NaHCO_3$, 2.3 mM $CaCl_2$, 5.6 mM D-glucose and 5 mM HEPES, pH 7.4) and then treated with 1 mL Locke's buffer containing either 2.5 μM ionomycin from a DMSO stock or DMSO alone (final DMSO concentration 0.1% v/v in both conditions) for 15 minutes at 37 °C, 5% CO_2. The supernatant was collected and aliquoted into a microtiter plate and mixed with either wildtype or 2G9C6 protein to a final concentration of approximately 50 μM. The microtiter plate was imaged by T_1-weighted MRI as for purified protein samples. 5HT concentrations were estimated from R_1 relaxation rates by fitting to a bimolecular equilibrium quadratic binding model with depletion, essentially as previously described[13]. Aliquots of the same supernatants were then assayed using a commercial colorimetric 5HT ELISA kit (IBL America, Minneapolis, MN), following the manufacturer's protocol.

Nuclear magnetic relaxation dispersion analysis

The longitudinal relaxation rates of purified BM3h solutions were measured at 25°C in the range of 10 kHz – 42.49 MHz using a SpinMaster FFC2000 1T C/DC (Stelar s.r.l., Italy) fast field-cycling nuclear magnetic resonance relaxometer. For T_1 measurements at field strengths greater than 12 MHz (0.281 T), sample magnetization equilibrated at the relaxation field before cycling to 16.2 MHz (0.383 T) for measurement of the magnetization after application of a 90°-flip-angle RF pulse. This process was repeated 15 times with the relaxation time varied from 0.01 to approximately $4T_1$. For relaxation fields less than 12 MHz, the sample was "pre-polarized" at a field strength of 25 MHz (0.587 T) for approximately $4T_1$ to compensate for diminished signal at lower fields.

Spin-lattice molar relaxivity, r_1, of ^{1}H in aqueous solutions of a paramagnetic metalloprotein is modeled as the sum (equation 3) of diamagnetic, r_d, and paramagnetic, r_p, molar relaxation rates,

$$r_1 = r_{1p} + r_{1d} + R_{1w},\qquad(3)$$

where R_w is the background relaxation rate of the aqueous solvent. The term r_{1p} is the molar form of the Solomon and Bloembergen equations (equation (4) and (5)):

$$r_{1p} = \left(\frac{c}{c+c_w}\right)\frac{q}{T_{1M}+\tau_M}\qquad(4)$$

$$\frac{1}{T_{1M}}=\frac{2}{15}\frac{\gamma_I^2 g^2\beta^2 S\,(S+1)}{r^6}\left(\frac{7\tau_c}{1+\omega_s^2\tau_c^2}+\frac{3\tau_c}{1+\omega_l^2\tau_c^2}\right)\tag{5}$$

In these equations, c is the molar concentration of paramagnetic ion; c_w is the molarity of water (55.5 M); T_{1M} is the relaxation time of water bound to the paramagnetic ion; q is the number of water molecules bound in the ion's first coordination sphere; r is the effective proton-ion distance for all bound water; ω_I and ω_S are the Larmor precession frequencies of proton nuclear spin, I, and the unpaired electron spin, S, respectively; γ_I is the ^{1}H gyromagnetic ratio; β is Bohr magneton; g is the free electron g-factor. The characteristic correlation time τ_c, of the two Lorentzian terms, is the sum of $\tau_c = \tau_M + \tau_S + \tau_R$, where these correlation times correspond to the bound water residence time, the frequency-independent electronic relaxation time, and the rotational correlation time of the overall complex, modeled with the Stokes-Einstein relation.

Prior work to estimate parameters governing proton relaxation in solutions of P450 homologues have been based primarily on temperature-dependent relaxation rate measurements at high NMR field strengths (200 - 600 MHz), at which rotational effects are minimal and the contribution of diamagnetic relaxation can be neglected. At the lower field strengths interrogated by field cycling relaxometers, the rotational correlation time becomes a significant contributor to solvent relaxation of metalloproteins, and therefore diamagnetic relaxation effects must be considered. Best fits to 25°C BM3h NMRD profiles (generally R^2 > 0.99) were achievable when the diamagnetic contribution to overall relaxation rates were removed using "model free" parameters in a three-term Lorentzian expansion previously fit to NMRD profiles obtained for apotransferrin[33]. Importantly, apotransferrin is a somewhat larger ~ 84 kDa protein, and the use of parameters for other diamagnetic proteins of lower molecular weight similar to BM3h was insufficient (R^2 < 0.9) to obtain acceptable parameter estimates using simple paramagnetic relaxation models based on the Solomon and Bloembergen theory. It should therefore be noted that we consider these parameter estimates to be useful for relative comparison of the mutants particularly under observation here. Parameter estimates were obtained using a nonlinear least squares fitting regression with scripts written in MATLAB. See the caption to Supplementary fig. 7 for additional details of assumptions used in the fitting procedure.

Supplementary Material

Refer to Web version on PubMed Central for supplementary material.

Acknowledgments

Abbreviations used

MRI	magnetic resonance imaging
DA	dopamine
5HT	serotonin (5-hydroxytryptamine)
NE	norepinephrine
BM3h	cytochrome P450-BM3 heme domain

References

1. Fukunaga M, et al. Layer-specific variation of iron content in cerebral cortex as a source of MRI contrast. Proc. Natl. Acad. Sci. USA. 2010; 107:3834–3839. [PubMed: 20133720]

2. Ahrens ET, Genove G, DeMarco U, Xu HY, Goins WF. A new transgene reporter for in vivo magnetic resonance imaging. Nat. Med. 2005; 11:450–454. [PubMed: 15778721]

3. Cohen B. MRI detection of transcriptional regulation of gene expression in transgenic mice. Nat. Med. 2007; 13:498–503. [PubMed: 17351627]

4. Lelyveld VS, Atanasijevic T, Jasanoff A. Challenges for Molecular Neuroimaging with MRI. Int. J. Imag. Syst. Tech. 2010; 20:71–79.

5. Ogawa S, Lee TM, Kay AR, Tank DW. Brain magnetic resonance imaging with contrast dependent on blood oxygenation. Proc. Natl. Acad. Sci. USA. 1990; 87:9868–9872. [PubMed: 2124706]

6. Jasanoff A. MRI contrast agents for functional molecular imaging of brain activity. Curr. Opin. Neurobiol. 2007; 17:593–600. [PubMed: 18093824]

7. Bloom JD, Labthavikul ST, Otey CR, Arnold FH. Protein stability promotes evolvability. Proc. Natl. Acad. Sci. USA. 2006; 103:5869–74. [PubMed: 16581913]

8. Fasan R, Meharenna YT, Snow CD, Poulos TL, Arnold FH. Evolutionary History of a Specialized P450 Propane Monooxygenase. J. Mol. Biol. 2008; 383:1069–1080. [PubMed: 18619466]

9. Sawayama AM, Chen MMY, Kulanthaivel P, Kuo M-S, Hemmerle H, Arnold FH. A Panel of Cytochrome P450 BM3 Variants to Produce Drug Metabolites and Diversify Lead Compounds. Chem.-Eur. J. 2009; 15:11723–11729. [PubMed: 19774562]

10. Ost TWB, Miles CS, Murdoch J, Cheung Y-F, Reid GA, Chapman SK, Munro AW. Rational re-design of the substrate binding site of flavocytochrome P450 BM3. FEBS Lett. 2000; 486:173–177. [PubMed: 11113461]

11. Weber E, Seifert A, Antonovici M, Geinitz C, Pleiss J, Urlacher VB. Screening of a minimal enriched P450 BM3 mutant library for hydroxylation of cyclic and acyclic alkanes. Chem. Commun. 2011; 47:944–946.

12. Modi S, Primrose WU, Boyle JM, Gibson CF, Lian LY, Roberts GC. NMR studies of substrate binding to cytochrome P450 BM3: comparisons to cytochrome P450 cam. Biochemistry. 1995; 34:8982–8. [PubMed: 7619797]

13. Shapiro MG, Westmeyer GG, Romero PA, Szablowski JO, Kuster B, Shah A, Otey CR, Langer R, Arnold FH, Jasanoff A. Directed evolution of a magnetic resonance imaging contrast agent for noninvasive imaging of dopamine. Nat. Biotech. 2010; 28:264–270.

14. Dauer W, Przedborski S. Parkinson's Disease: Mechanisms and Models. Neuron. 2003; 39:889–909. [PubMed: 12971891]

15. Miwa, Julie M.; Freedman, R.; Lester, Henry A. Neural Systems Governed by Nicotinic Acetylcholine Receptors: Emerging Hypotheses. Neuron. 2011; 70:20–33. [PubMed: 21482353]

16. Schultz W. Multiple dopamine functions at different time courses. Annu. Rev. Neurosci. 2007; 30:259–88. [PubMed: 17600522]

17. aan het Rot M, Mathew SJ, Charney DS. Neurobiological mechanisms in major depressive disorder. CMAJ. 2009; 180:305–313. [PubMed: 19188629]

18. Canli T, Lesch K-P. Long story short: the serotonin transporter in emotion regulation and social cognition. Nat. Neurosci. 2007; 10:1103–1109. [PubMed: 17726476]

19. Haines DC, Tomchick DR, Machius M, Peterson JA. Pivotal role of water in the mechanism of P450BM-3. Biochemistry. 2001; 40:13456–65. [PubMed: 11695892]

20. Girvan HM, Seward HE, Toogood HS, Cheesman MR, Leys D, Munro AW. Structural and Spectroscopic Characterization of P450 BM3 Mutants with Unprecedented P450 Heme Iron Ligand Sets. J. Biol. Chem. 2007; 282:564–572. [PubMed: 17077084]

21. Joyce MG, Girvan HM, Munro AW, Leys D. A single mutation in cytochrome P450 BM3 induces the conformational rearrangement seen upon substrate binding in the wild-type enzyme. J. Biol. Chem. 2004; 279:23287–93. [PubMed: 15020590]

22. Jennings WB, Farrell BM, Malone JF. Attractive intramolecular edge-to-face aromatic interactions in flexible organic molecules. Acc. Chem. Res. 2001; 34:885–94. [PubMed: 11714260]

23. Thomas A, Meurisse R, Brasseur R. Aromatic side-chain interactions in proteins. II. Near- and far-sequence Phe-X pairs. Proteins. 2002; 48:635–44. [PubMed: 12211031]

24. Turner JM, Graziano J, Spraggon G, Schultz PG. Structural plasticity of an aminoacyl-tRNA synthetase active site. Proc. Natl. Acad. Sci. USA. 2006; 103:6483–8. [PubMed: 16618920]

25. Landwehr M, Hochrein L, Otey CR, Kasrayan A, Backvall JE, Arnold FH. Enantioselective alpha-hydroxylation of 2-arylacetic acid derivatives and buspirone catalyzed by engineered cytochrome P450 BM-3. J. Am. Chem. Soc. 2006; 128:6058–9. [PubMed: 16669674]

26. Peters MW, Meinhold P, Glieder A, Arnold FH. Regio- and Enantioselective Alkane Hydroxylation with Engineered Cytochromes P450 BM-3. J. Am. Chem. Soc. 2003; 125:13442–13450. [PubMed: 14583039]

27. Reetz MT, Prasad S, Carballeira JD, Gumulya Y, Bocola M. Iterative saturation mutagenesis accelerates laboratory evolution of enzyme stereoselectivity: rigorous comparison with traditional methods. J. Am. Chem. Soc. 2010; 132:9144–52. [PubMed: 20536132]

28. Kim TD, Eddlestone GT, Mahmoud SF, Kuchtey J, Fewtrell C. Correlating Ca2+ Responses and Secretion in Individual RBL-2H3 Mucosal Mast Cells. J. Biol. Chem. 1997; 272:31225–31229. [PubMed: 9395446]

29. Weintraub WH, Cleveland-Wolfe P, Fewtrell C. Paracrine Ca2+ signaling in vitro: serotonin-mediated cell-cell communication in mast cell/smooth muscle cocultures. J. Cell. Physiol. 1994; 160:389–99. [PubMed: 8040194]

30. Maiti S, Shear JB, Williams RM, Zipfel WR, Webb WW. Measuring Serotonin Distribution in Live Cells with Three-Photon Excitation. Science. 1997; 275:530–532. [PubMed: 8999797]

31. Brainard GC, Hanifin JP, Greeson JM, Byrne B, Glickman G, Gerner E, Rollag MD. Action spectrum for melatonin regulation in humans: evidence for a novel circadian photoreceptor. J Neurosci. 2001; 21:6405–12. [PubMed: 11487664]

32. Griessenauer CJ, Chang SY, Tye SJ, Kimble CJ, Bennet KE, Garris PA, Lee KH. Wireless Instantaneous Neurotransmitter Concentration System: electrochemical monitoring of serotonin using fast-scan cyclic voltammetry--a proof-of-principle study. J. neurosurg. 2010; 113:656–65. [PubMed: 20415521]

33. Bertini I, Fragai M, Luchinat C, Parigi G. 1H NMRD profiles of diamagnetic proteins: a model-free analysis. Magn. Reson. Chem. 2000; 38:543–550.

34. Bloembergen N. Proton Relaxation Times in Paramagnetic Solutions. J. Chem. Phys. 1957; 27:572.

35. Solomon I. Relaxation Processes in a System of Two Spins. Phys. Rev. 1955; 99:559–565.

36. Modi S, Primrose WU, Boyle JMB, Gibson CF, Lian L-Y, Roberts GCK. NMR Studies of Substrate Binding to Cytochrome P450 BM3: Comparisons to Cytochrome P450 cam. Biochemistry. 1995; 34:8982–8988. [PubMed: 7619797]

37. Goldfarb D, Bernardo M, Thomann H, Kroneck PMH, Ullrich V. Study of Water Binding to Low-Spin Fe(III) in Cytochrome P450 by Pulsed ENDOR and Four-Pulse ESEEM Spectroscopies. J. Am. Chem. Soc. 1996; 118:2686–2693.

38. Sligar SG. Coupling of spin, substrate, and redox equilibriums in cytochrome P450. Biochemistry. 1976; 15:5399–5406. [PubMed: 187215]

39. Ewing AG, Bigelow JC, Wightman RM. Direct in vivo monitoring of dopamine released from two striatal compartments in the rat. Science. 1983; 221:169–71. [PubMed: 6857277]

40. Siegel J, Zanghellini A, Lovick H, Kiss G. Computational Design of an Enzyme Catalyst for a Stereoselective Bimolecular Diels-Alder Reaction. Science. 2010; 329:309–313. [PubMed: 20647463]

41. Dunitz JD. The entropic cost of bound water in crystals and biomolecules. Science. 1994; 264:670. [PubMed: 17737951]

42. Setny P, Baron R, McCammon JA. How Can Hydrophobic Association Be Enthalpy Driven? J. Chem. Theory Comput. 2010; 6:2866–2871. [PubMed: 20844599]

43. Baron R, Setny P, McCammon JA. Water in cavity-ligand recognition. J. Am. Chem. Soc. 2010; 132:12091–7. [PubMed: 20695475]

44. Khersonsky O, Tawfik D. Enzyme Promiscuity: A Mechanistic and Evolutionary Perspective. Annu. Rev. Biochem. 2010; 79:471–505. 2010. [PubMed: 20235827]

45. Lelyveld VS, Brustad E, Arnold FH, Jasanoff A. Metal-Substituted Protein MRI Contrast Agents Engineered for Enhanced Relaxivity and Ligand Sensitivity. J. Am. Chem. Soc. 2011; 133:649–651. [PubMed: 21171606]

46. Fisher CW, Caudle DL, Martin-MartinWixtrom C, Quattrochi LC, Tukey RH, Waterman MR, Estabrook RW. High-level expression of functional human cytochrome P450 1A2 in Escherichia coli. FASEB J. 1992; 6:759–64. [PubMed: 1537466]

47. Muchmore, DC.; McIntosh, LP.; Russell, CB.; Anderson, DE.; Dahlquist, FW. [3] Expression and nitrogen-15 labeling of proteins for proton and nitrogen-15 nuclear magnetic resonance. In: Norman, JO.; Thomas, LJ., editors. Methods Enzym. Vol. 177. Academic Press; 1989. p. 44-73.

48. Santi DV, Reisinger SJ, Patel KG. Total synthesis of multi-kilobase DNA sequences from oligonucleotides. Nat. Prot. 2006; 1:2596–2603.

49. Omura T, Sato R. The Carbon Monoxide-Binding Pigment of Liver Microsomes. Ii. Solubilization, Purification, and Properties. J. Biol. Chem. 1964; 239:2379–85. [PubMed: 14209972]

50. Otey CR. High-throughput carbon monoxide binding assay for cytochromes p450. Methods Mol. Biol. 2003; 230:137–9. [PubMed: 12824576]

51. Schenkman JB, Remmer H, Estabrook RW. Spectral studies of drug interaction with hepatic microsomal cytochrome. Mol. Pharm. 1967; 3:113–23.

52. Hosea NA, Miller GP, Guengerich FP. Elucidation of distinct ligand binding sites for cytochrome P450 3A4. Biochemistry. 2000; 39:5929–39. [PubMed: 10821664]

53. Kabsch W. Xds. Acta crystallogr. D, Biol. crystallogr. 2010; 66:125–32. [PubMed: 20124692]

54. Evans P. Scaling and assessment of data quality. Acta crystallogr. D, Biol. crystallogr. 2006; 62:72–82. [PubMed: 16369096]

55. Vagin A, Teplyakov A. MOLREP: an automated program for molecular replacement. J. App. Crystallogr. 1997; 30:1022–1025.

56. Bailey S. The Ccp4 Suite - Programs for Protein Crystallography. Acta crystallogr. D, Biol. crystallogr. 1994; 50:760–763. [PubMed: 15299374]

57. Emsley P, Cowtan K. Coot: model-building tools for molecular graphics. Acta crystallogr. D, Biol. crystallogr. 2004; 60:2126–2132. [PubMed: 15572765]

58. Murshudov GN, Vagin AA, Dodson EJ. Refinement of Macromolecular Structures by the Maximum-Likelihood Method. Acta crystallogr. D, Biol. crystallogr. 1997; 53:240–255. [PubMed: 15299926]

59. Adams PD, et al. PHENIX: a comprehensive Python-based system for macromolecular structure solution. Acta crystallogr. D, Biol. crystallogr. 2010; 66:213–221. [PubMed: 20124702]

60. Griffin BW, Peterson JA. Pseudomonas putida cytochrome P-450. The effect of complexes of the ferric hemeprotein on the relaxation of solvent water protons. J. Biol. Chem. 1975; 250:6445–6451. [PubMed: 1158868]

61. Jacobs RE, Singh J, Vickery LE. NMR studies of cytochrome P-450scc. Effects of steroid binding on water proton access to the active site of the ferric enzyme. Biochemistry. 1987; 26:4541–4545. [PubMed: 3663605]

62. Modi S, Paine MJ, Sutcliffe MJ, Lian LY, Primrose WU, Wolf CR, Roberts GC. A model for human cytochrome P450 2D6 based on homology modeling and NMR studies of substrate binding. Biochemistry. 1996; 35:4540–50. [PubMed: 8605204]

63. Philson SB, Debrunner PG, Schmidt PG, Gunsalus IC. The effect of cytochrome P-450cam on the NMR relaxation rate of water protons. J. Biol. Chem. 1979; 254:10173–10179. [PubMed: 226536]

64. Li Y, Drummond DA, Sawayama AM, Snow CD, Bloom JD, Arnold FH. A diverse family of thermostable cytochrome P450s created by recombination of stabilizing fragments. Nat. Biotech. 2007; 25:1051–1056.

- Cytochrome P450-BM3 demonstrates ligand-dependent MRI contrast enhancements.

- Directed evolution rapidly improves P450-BM3 affinity for dopamine and serotonin.

- X-ray crystallography shows the structural basis of improved ligand binding.

- Broadly specific sensors show overlapping ligand orientations in the active site.

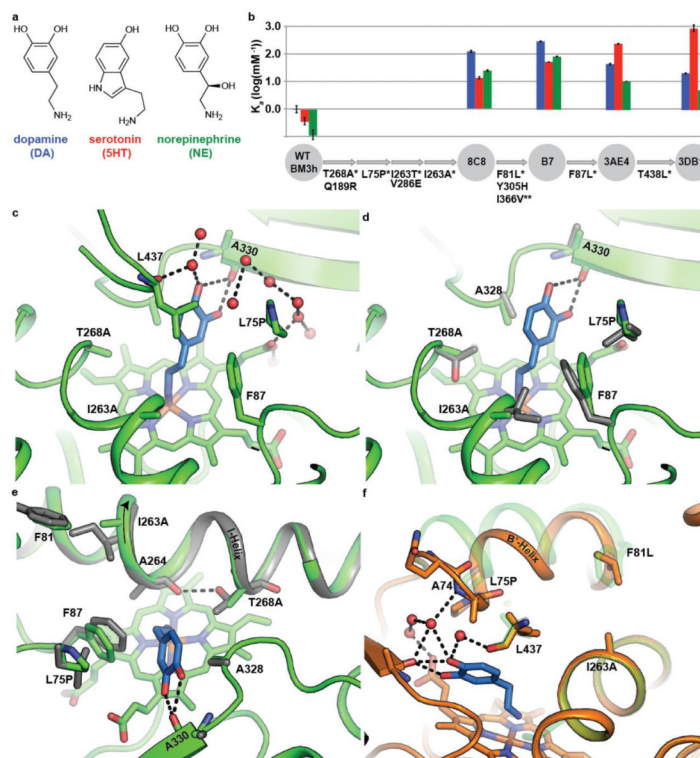- Highly specific sensors use unique binding modalities to increase specificity.

Figure 1. Directed evolution and structural characterization of broadly specific DA sensors
(a) Structures of dopamine (DA), serotonin (5HT) and norepinephrine (NE). (b) Color-coded bar graphs show affinity constants (K_a) for DA, 5HT and NE of error-prone PCR BM3h-B7 lineage from Ref. 12. Bars correspond to: DA (blue, left), 5HT (red, middle) and NE (green, right). We have set the Y-axis in units of $\log(mM^{-1})$; for reference to table 1, the 0 axis would correspond to a dissociation constant (K_d) of 1 mM. Bar graphs descending below the 0 axis indicate dissociation constants that exceed 1 mM. Residues located in the active site of BM3h are marked (*). Mutations identified by ** were included to improve protein stability. Errors for K_a bar graphs are reported as standard deviations determined from a minimum of three independent experiments. (c) DA (blue) bound to BM3h-8C8 (green). Waters are shown as red spheres and dashed lines indicate hydrogen bonds. The exocyclic hydroxyls of DA form hydrogen bonds to the backbone carbonyl of A330. (d) Active site alignment of BM3h-8C8 + DA (green) and wild type BM3h (grey, from PDB:2IJ2).[20] Mutation at L75P allows movement of F81 to accommodate the DA ring (blue). (e) Rotation of the I-helix (shown by arrow) due to mutation at T268A. An alignment of the wild type (grey) and BM3h-8C8 + DA (green) is shown. A dashed line marks the wild type hydrogen bond between the side-chain T268 and the backbone carbonyl of A264. The rotation of the I-helix can be readily observed by comparing the Cα positions of wild type I263 and I263A in BM3h-8C8. (f) Large scale movements in the B'-Helix upon mutation of F81 in the BM3h-8C8 (green) to leucine in BM3h-B7 (orange). BM3h-B7 bound DA is shown in blue.
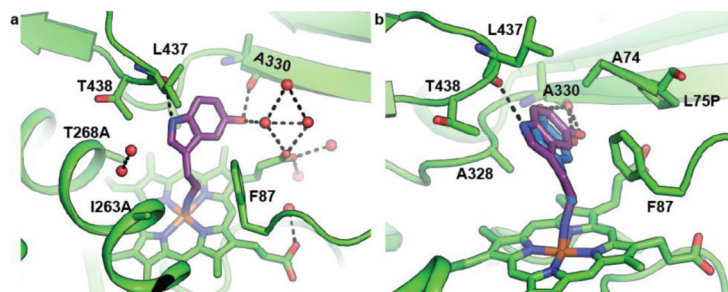
Figure 2. Shared binding modalities in broadly specific DA/5HT binder BM3h-8C8
(a) BM3h-8C8 bound 5HT (purple) shares interactions that are used for DA binding modes observed in fig. 1. The exocyclic hydroxyl forms a hydrogen bond with the backbone carbonyl of A330 as well as an existing water network. The indole nitrogen forms a hydrogen bond to the backbone carbonyl of L437. Hydrogen bonds are shown by dashed lines and waters by red spheres. (b) The aromatic rings of 5HT and DA point into the same binding pocket towards A330. 5HT is shown in purple overlaid with DA, shown in blue. In both cases the neurotransmitter amine coordinates the heme iron center.
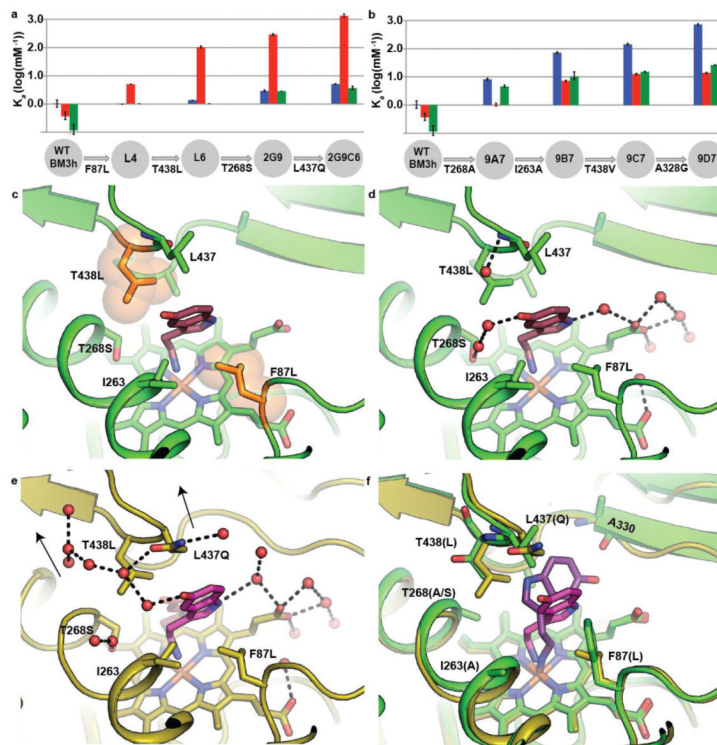
Figure 3. Directed evolution and structural characterization of highly specific 5HT and DA sensors

(a-b) Color-coded bar graphs show affinity constants (K_a) for DA, 5HT and NE as described in fig. 1. (a) 5HT-selective BM3h-2G9C6 lineage evolved using active site-directed libraries. (b) DA-selective BM3h-9D7 lineage evolved using active site-directed libraries. (c) 5HT (dark red) bound to BM3h-2G9 (green backbone). Active site mutations F87L and T438L (orange), shown as sticks and van der Waals spheres, provide the hydrophobic packing core that sandwiches the 5HT ligand. T268S is also shown; deletion of the Cγ methyl group accommodates the 5HT ethylamine moiety. (d) A network of waters connects the 5HT exocyclic hydroxyl and the side-chain of T268S. A 2nd network of waters links the indole nitrogen and the propionic acid side-chain of the heme. (e) Crystal structure of BM3h-2G9C6 (gold) bound to 5HT (pink). A slight rotation in the bound 5HT compared to BM3h-2G9 (transparent ligand) is observed as a result of the L437Q mutation. An extensive water hydrogen bonding network linking L437Q and 5HT is also shown (red spheres and dashed lines). Arrows indicate 2 of the 3 main solvent channels in BM3h. (f) A comparison of 5HT orientations in broadly specific BM3h-8C8 (green protein, purple 5HT) and BM3h-2G9C6 (gold protein, pink 5HT). 5HT occupies an alternative pocket within the BM3h active site in 5HT-selective BM3h-2G9C6. In panels b and d, waters are shown as red spheres and dashed lines indicate hydrogen bonds. Errors for K_a bar graphs are reported as standard deviations determined from a minimum of three independent experiments.
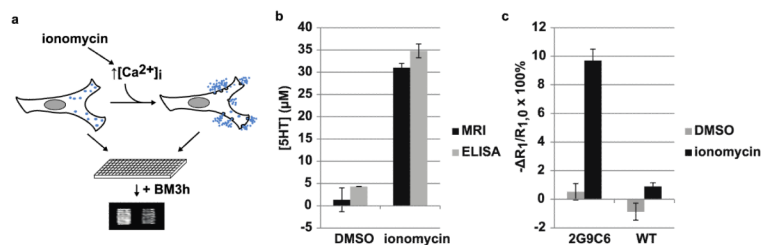
Figure 4. BM3h-2G9C6 is a sensor for secreted 5HT in cell culture
(a) RBL-2H3 cells secrete 5HT in response to increases in intracellular Ca^{2+} concentration (e.g. by treatment with ionomycin), which can then be observed by T_1-weighted MRI of aspirated treatment medium mixed with purified BM3h protein in microtiter plate wells. The image illustrates an example contrast-adjusted T_1-weighted spin echo scan (TE = 10 ms, TR = 1221 ms) of a 2-mm slice of microtiter wells containing, left, DMSO-treated cell supernatant or, right, ionomycin-treated cell supernatant, both mixed with BM3h-2G9C6 to a final concentration of 50 µM. (b) Estimates of absolute 5HT concentration in aspirated treatment medium from 80 – 90% confluent 75-cm^2 flasks 15 minutes after treatment with Locke's buffer containing either 0.1% (v/v) DMSO or 2.5 µM ionomycin. Briefly, clarified supernatant was either mixed with purified BM3h-2G9C6 and observed by T_1-weighted MRI or assayed for 5HT content using a commercial colorimetric ELISA kit. (c) Aliquots of the same samples as in (b) were imaged by MRI after addition of 50 µM BM3h wild type (WT) or BM3h-2G9C6 protein. Longitudinal relaxation rates (R_1) of BM3h-containing samples are expressed as $-\Delta R_1/R_{1,0} = (R_{1,0} - R_{1,15})/R_{1,0} \times 100\%$, where $R_{1,0}$ and $R_{1,15}$ are the relaxation rates of Locke's buffer containing BM3h protein and either DMSO or 2.5 µM ionomycin before or after 15 minutes of exposure to cells, respectively. Errors are reported as standard deviations determined from a minimum of three independent experiments.
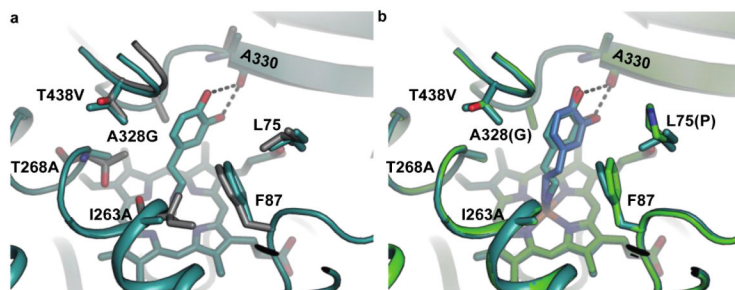
Fig. 5. Alternative dopamine binding in BM3h-9D7
(a) Active site alignment of BM3h-9D7 + DA (teal) and wild type BM3h (grey, from PDB: 2IJ2)[20] shows no change in F87 orientation. (b) Active site alignment of BM3h-8C8 + DA (green) and BM3h-9D7 + DA (teal). Differences in DA ligand orientation are due to mutations at L75P (BM3h-8C8) or A330G (BM3h-9D7), which allow improved packing of F87 against the DA catechol ring. Residue identities in parentheses represent mutations that differ in BM3h-9D7 and BM3h-8C8.

Table 1

Summary of characteristics for BM3h variants described in this paper, including mutation identity, dissociation constant (K_d), relaxivity in the absence of ligand (r_1), r_1 in the presence of saturating ligand (1 – 2 mM) denoted after the slash (r_1 / ligand bound), and thermostability.

Variant	mutations	K_D (μM)			r_1	r_1 / ligand bound	T_{50}(°C)
		DA	5HT	NE	(mm^{-1}s^{-1})	(mm^{-1}s^{-1})	
BM3h	None	970 ± 250 [a]	2700 ± 800 [a]	8600 ± 3200 [a]	1.23 ± 0.07 [a]	0.76 [a] / DA	54.9 [c]
BM3h-8C8 [b]	T268A, L75P, I163A, Q189R, V286E	8.9 ± 0.7 [a,b]	80 ± 8 [a,b]	44 ± 3 [a]	1.1 ± 0.1 [a]	0.17 [a] / DA	8.6
BM3h-B7	T268A, L75P, I163A, F81L, Q189R, V286E, Y395H, I366V	3.3 ± 0.1 [a]	18.6 ± 0.1 [a]	11.8 ± 0.4 [a]	0.96 ± 0.13 [a]	0.14 [a] / DA	47.6
BM3h-3AE4	T268A, L75P, I163A, F81L, Q189R, V286E, Y395H, I366V, F87L	21.4 ± 1.3		91.3 ± 0.2			n.d
BM3h-3DB10	T268A, L75P, I163A, F81L, Q189R, V286E, Y395H, I366V, F87L, T438L	46.1 ± 1.7	1.1 ± 0.3	190 ± 30	0.73 ± 0.05	0.22 / 5HT	43.9
BM3h-L4		<1000	199 ± 1	n.b.d.	1.55 ± 0.14	1.1 / 5HT	59.3
BM3h-L5	T438L	<1000	<1000	n.b.d.	n.d.	n.d.	n.d.
BM3h-L6		<750	9.3 ± 0.1	n.b.d	1.44 ± 0.12	0.31 / 5HT	55.6
BM3h-2G9 [b]	F87L, T438L, T268S [d]	347 ± 26	3.3 ± 0.2 [b]	<350	1.27 ± 0.11	n.d.	53.2
BM3h-2G9C6 [b]	F87L, T438L, T268S, L437Q [d]	198 ± 7	0.7 ± 0.1 [b]	275 ± 40	1.89 ± 0.02	0.14 / 5HT	53.6
BM3h-9A7	T268A	120 ± 10	960 ± 110	210 ± 24	1.66 ± 0.05	0.43 / DA	57.2
BM3h-9B7	T268A, I263A	13.1 ± 0.9	136 ± 8	94 ± 30	1.46	0.14 / DA	57.8
BM3h-9C7	T268A, I263A, T438V	6.6 ± 0.5	77 ± 5	64 ± 3	1.29 ± 0.05	0.13 / DA	56.9
BM3h-9D7 [b]	T268A, I263A, T438V, A328G	1.3 ± 0.1 [b]	70 ± 3	37 ± 1	1.31 ± 0.07	0.07 / DA	54.6
BM3h-L75P	T268A, L75P, I263A	6.2 ± 0.5	33 ± 1	28 ± 3	1.64 ± 0.02	0.14 / DA	52

n.b.d. – no binding detected

n.d. – not determined

Errors for K_d and r_1 are reported as standard deviations determined from a minimum of three independent experiments.

[a] Taken from Ref. 12

[b] Crystal structures are available from this work

[c] Taken from Ref. 60

[d]An additional mutation at R51C was observed due to polymerase error. Reversion of this mutation did not greatly affect the observed binding and relaxivity.